Dalton Transactions

PAPER

View Article Online
View Journal

Cite this: DOI: 10.1039/c7dt04063f

Gallic acid-assisted synthesis of Pd uniformly anchored on porous N-rGO as efficient electrocatalyst for microbial fuel cells†

Xiao-Tong Wu, Jie-Cheng Li, Qiu-Ren Pan, Nan Li * and Zhao-Qing Liu *

Received 28th October 2017,
Accepted 18th December 2017

DOI: 10.1039/c7dt04063f

rsc.li/dalton

The sluggish kinetic rate-limiting oxygen reduction reaction (ORR) at the cathode remains the foremost issue hindering the commercialization of microbial fuel cells (MFCs). Utilization of the effect of micromolecule conjugation and the synergistic effect between Pd nanoparticles and N-rGO (nitrogen-doped reduced graphene oxide) to stabilize a precious metal onto carbon materials is a promising strategy to design and synthesize highly efficient cathode catalysts. In this study, gallic acid is used to facilitate the coupling of palladium (Pd) with N-rGO to form GN@Pd-GA *via* a simple hydrothermal process. Notably, the as-synthesized GN@Pd-GA as a cathode catalyst shows an approximately direct four-electron feature and demonstrates a high ORR performance in 0.1 M KOH. Furthermore, the stability and methanol tolerance of GN@Pd-GA are superior to those of the commercial Pt/C catalysts. In addition, a maximum power density of 391.06 ± 0.2 mW m^{-2} of MFCs equipped with GN@Pd-GA was obtained, which was 96.2% of the power density of MFCs equipped with a commercial Pt/C catalyst.

1 Introduction

Excessive consumption of fossil fuels has exacerbated the current energy crisis and environmental pollution, and there is an urgent need to explore renewable and sustainable energy technologies.[1–3] As ideal renewable energy devices, microbial fuel cells (MFCs) connect energy and wastewater since they can harvest electric energy from metabolic processes of bacteria and further solve the problem of environment pollution from sewage.[2–4] However, the relatively low power density of MFCs greatly limit their practical applications.[5] Specifically, a major barrier to increasing the power density of MFCs is the ORR efficiency (the reductive half reaction O_2/OH^- of the cathodic reaction, *e.g.*, in alkaline media) on the air-cathode.[6,7] As such, sluggish kinetics of the ORR largely restricts the rate of energy conversion in the MFCs.[8] To date, the best ORR performance of cathode catalysts is generally demonstrated by Pt-based catalysts such as Pt–Ni alloys,[9,10] PtPd alloys,[11,12] and PtFe nanoparticles.[13,14] Among them, PtM[15,16] alloys can minimize the overpotential and promote fast reaction kinetics of ORR for MFCs.[17–19] However, the formation of disorder PtM cores and low dispersity of active tensile strain on Pt (111) facet hinder long-term stability of Pt-based catalysts after exposing to acidic electrolyte solution.[20] Alternatively, Pd and its derivatives, which are relatively affordable due to their earth-abundance and have comparatively high catalytic activities and stabilities, have recently attracted significant attention as cathode catalysts.[21,22] For example, Wang and co-workers successfully inlayed Pd nanoparticles within a Pt icosahedron, thus enhancing the ORR performance significantly by designing a defective structure for cost-effective catalysts.[12,23] Despite the fact that Pd-based compounds exhibit high performance in electrocatalytic processes, the scarcity and high dosage requirements of Pd severely limit its practical applications.[24,25]

Encouragingly, an effective strategy to enhance the catalytic efficiency and stability is to introduce carbon materials (*e.g.*, carbon nanotubes, carbon nanowires, and carbon plates), which have been identified as potential conductive materials.[26–28] Among them, graphene and its derivatives (N or S-doped graphene) have been widely applied in energy conversion and storage owing to their low internal resistance and high activity and conductivity.[29,30] Obviously, heteroatom (N, P, or S)-doped carbon-based materials can serve as alternatives with highly efficiency and low-cost to Pd-based catalysts for the ORR.[31] However, the complicated synthetic process and harsh reaction

School of Chemistry and Chemical Engineering/Guangzhou Key Laboratory for Environmentally Functional Materials and Technology/Key Laboratory for Water Quality and Conservation of the Pearl River Delta, Ministry of Education, Guangzhou University, Guangzhou 510006, PR China. E-mail: nanli@gzhu.edu.cn, lzqgzu@gzhu.edu.cn; Tel: +86-20-39366908; Fax: +86-20-39366908

† Electronic supplementary information (ESI) available: Tables S1–S3. See DOI: 10.1039/c7dt04063f

conditions greatly limit their further applications. Therefore, it is imperative to design and develop efficient and stable electrocatalysts for MFCs by a simple, easy, and scalable strategy.[32]

Recently, a biomolecule-assisted strategy to construct metal nanoparticles with high dispersities has become a hot topic of research.[33] Accordingly, in this study, gallic acid-assisted Pd nanoparticles decorated on N-doped porous graphene have been successfully developed by a simple process. Impressively, the as-synthesized catalyst exhibits excellent ORR performance with a large limited current density (-4.03 mA cm^{-1}) and a positive onset potential (-0.101 V *vs.* SCE), close to that of the bench mark noble metal catalyst Pt/C. An in-depth study shows that the high ORR performance of Pd/N-rGo is mainly ascribed to the synergistic effect between Pd nanoparticles and N-rGo, in which the porous N-doped graphene provides a conductive surface area and abundant active sites to facilitate the charge transfer efficiency, and the channels for electrolyte diffusion to the Pd nanoparticles are retained. This finding will provide a new path for the development of a highly efficient and stable ORR catalyst for MFCs.

2 Experimental

2.1 Synthesis of silicon dioxide (SiO_2) spheres

Regular silicon spheres were synthesized by the polymerization method. Typically, an aqueous-alcoholic solution was prepared by mixing 150 mL of ethanol with 20 mL of distilled water. Subsequently, 8 mL of ammonium hydroxide was added under vigorous stirring (bottle A). Then, 10 mL of tetraethoxysilane (TEOS) was added to 60 mL of ethanol to form the precursor solution (bottle B). After stirring the contents of both bottles for 15 min, the contents of bottle B were added rapidly to bottle A under slow stirring until flocculent materials appeared at 30 °C and kept for 6 h.

2.2 Synthesis of graphene oxide (GO)

Graphene oxide was synthesized according to the modified Hummers methods reported in the literature.[34] Briefly, graphite carbon (1.0 g) and $NaNO_3$ (500 mg) were added consecutively to a round-bottom flask containing 23 mL concentrated sulfuric acid (H_2SO_4). The mixture was then poured into an ice bath water and stirred evenly. $KMnO_4$ (3.0 g) was then slowly added to the mixture. As the solution turned dark green, the mixture was added to 45 mL distilled water before being heated to 35 °C under constant stirring for 30 min; subsequently, the container was transferred to a water bath at 70 °C, and the temperature was increased to 98 °C over 15 min. The solution was then added to a mixture of H_2O (140 mL) and 30% H_2O_2 (10 mL). The 250 mL graphene oxide (4 mg mL^{-1}) aqueous dispersion was obtained by means of stratification, separation and abstersion until the value of pH equalled to 7. The utilized GO solution should undergo drastic ultrasonic dispersion each time.

2.3 Synthesis of porous nitrogen-doped graphene

Porous nitrogen-doped graphene was prepared by a hard template method. To dope the graphitic framework with N, 25 mL of the as-prepared GO aqueous dispersion (4 mg mL^{-1}) was mixed with 75 mL distilled water by sonication for 2 h to form a GO aqueous solution of low concentration (1 mg mL^{-1}). A solution containing both 1.0 g SiO_2 spheres and 2.0 g cetyltrimethylammonium bromide (CTAB) was stirred for 4 h at room temperature. Then, the filter residue was dried at 50 °C for 12 h. Afterward, urea with mass ratio of 1 : 2 was added in the powder (GO@SiO_2), and the mixture was ground and transferred into a porcelain boat and annealed at 800 °C for 4 h under a N_2 atmosphere. Finally, the powder was further treated by alkali etching (6 M KOH) to obtain porous structural nitrogen-doped reduced graphene oxide (GN). In addition, porous graphene (G) was obtained *via* the abovementioned method without adding urea.

2.4 Synthesis of Pd-anchored porous nitrogen-doped graphene

The as-synthesized 20 mg GN and G were respectively dispersed in 20 mL distilled water to form two suspension solutions, which were mixed with 0.96 mL $Pd(NH_3)_4Cl_2$ (11.3 mg mL^{-1}) and kept at 60 °C for 15 min. Moreover, $Pd(NH_3)_4Cl_2$ solution was prepared using $PdCl_2$ (0.82 g), which was dissolved in 5 mL HCl (5%), and then, $NH_3{\cdot}H_2O$ (25%–30%) was added dropwise to obtain the pink turbid liquid. The 11.30 mg mL^{-1} $Pd(NH_3)_4Cl_2$ solution was then mixed with distilled water in a 100 mL volumetric flask while steadily adding $NH_3{\cdot}H_2O$ (observation: the pink liquid transformed into a transparent solution). Next, 10 mL gallic acid (GA) (1.43 mg mL^{-1}) was added dropwise to the suspension that was then kept at 60 °C for 15 min; 5 mL hydrazine hydrate (80%) was added to *in situ* restored Pd at 60 °C for 6 h. The powders formed were separated out of the solution by vacuum suction filtration and dried at 50 °C for 12 h, which were denoted as GN@Pd-GA and G@Pd-GA. Moreover, GN-doped Pd was prepared without adding gallic acid and denoted as GN@Pd.

2.5 Construction and operation of the MFCs

In this study, a single-chamber air-cathode MFC device was used, with a liquid volume of 28 mL.[35] The anode was pretreated by dipping a bare carbon cloth in an acetone solution before annealing it at 500 °C for 30 min (after drying). The air-cathode was also fabricated by covering a certain amount of the as-prepared catalyst materials (3 mg cm^{-2}) or Pt/C catalyst (wt 20%, 2.5 mg cm^{-2}) on the carbon cloth, and the effective area of both the anode and the cathode was measured to be approximately 7 cm^{-2}. A Ti (titanium) wire was used to connect both ends of the electrode with an external resistance (1000 Ω). The activate matter obtained from the downstream Pearl River ecosystem. Importantly, the culture medium consists of a mixture of glucose (1 g L^{-1}), trace elements (12.5 mL), vitamin solution (5 mL) and phosphate-buffered nutrient medium (pH = 7.0) containing NH_4Cl (0.31 g L^{-1}),

$NaH_2PO_4{\cdot}H_2O$ (1.30 g L^{-1}), $Na_2HPO_4{\cdot}3H_2O$ (9.4 g L^{-1}), and KCl (0.13 g L^{-1}).[32,36] A 16-channel data acquisition system (MPS 010602, Beijing) was used to obtain the output voltage of the MFCs for different cathode materials (per minute). Moreover, the polarization curves of different cathodes were acquired by adjusting the external circuit resistance from 40 Ω to 5000 Ω, and the anode electrode potentials were measured by inserting a saturated calomel electrode (SCE) electrode to compose a two-electrode system. By means of the formula $P = V \times I$, the power density P could be calculated. Both I and P were normalized to the effective area of the cathode surface, and the current density I was calculated using the formula: $I = V$ (cell voltage)/$(R \times A)$ (external resistance and effective area).

2.6 Characterization

The surface morphology and crystal microstructure of the as-prepared GN@Pd-GA composites were analyzed by field emission scanning electron microscopy (FE-SEM, JEOL JSM-7001F) and transmission electron microscopy (TEM, JEM2010-HR). The crystal structure of the materials was elucidated by Bruker, D8 ADVANCE. The surface oxidation states were analyzed using a Fourier transform infrared spectrometer (FTIR, Tensor 27, 400–4000 cm^{-1}). The specific surface area and pore size distribution of the samples were investigated by the Brunauer–Emmett–Teller (BET) method.

2.7 Electrochemical measurements

The ORR performance of the samples was evaluated by the CHI 760D electrochemical workstation (Shanghai, Chenhua) with a rotating disk electrode (RDE) system: the experiments were performed in a standard three-electrode system, with a saturated calomel electrode (SCE) as the reference electrode, a glassy carbon electrode as the counter electrode, and the catalyst film coated on a rotating disk electrode (~0.1 mg cm^{-3} loaded on the electrode surface) as the working electrode. A 0.1 mol L^{-1} KOH electrolyte solution was used for the ORR tests (in an alkaline solution). The RDE system was used for gaining insights into the electron transfer under oxygen reduction, where the rotational speed was varied from 400 to 2500 rpm at a scan rate of 10 mV s^{-1}.

Herein, Koutecky–Levich (K–L) curve analysis was used to calculate the number of electrons transferred (n) using the following formula:[37]

$$j^{-1} = j_k{}^{-1} + (0.62nFAD^{2/5}V^{-1/6}C)^{-1}\omega^{-1/2} \quad (1)$$

In this formula, j represents the measured current (A), F is the Faraday constant (96 485 C mol^{-1}), A represents the effective area of the disk electrode (0.126 cm^2), D is the diffusion rate of oxygen, V represents the kinematic viscosity, C is the oxygen concentration in the electrolyte, and ω represents the rotation rate of the electrode.[38] After data collection, working electrodes were prepared to conduct a steady-state potential sweep from open-circuit voltage in both a positive direction (+0.05 V) and negative direction (−0.05 V) in an O_2-saturated 0.1 M KOH solution. The cyclic voltammograms (CV) were obtained at the rates ranging from 50 mV s^{-1} to 2 mV s^{-1}. The electrochemically active surface area (ECSA) of the catalyst was determined using an electrical double-layer capacitor (C_{DL}).[39,40] C_{DL} curves could be used to obtain every intermediate point of voltage by linear fitting under different scanning speeds. Herein, the ECSA analysis was conducted by the following formula:

$$\text{ECSA} = C_{DL}/C_s \quad (2)$$

In this formula, C_{DL} represents the double layer capacitance and C_s represents the specific capacitance. We have discussed the ECSA through the values of C_{DL} due to the linearity between them.[41,42]

Results and discussion

The synthesis process of GN@Pd-GA material is shown in Scheme 1. Primarily, the Pd^{2+} complex encircles the as-prepared nitrogen-doped carbon spheres. The added gallic acid contains acidic functional groups (–COO, –O) and a benzene moiety, which absorbs metal ions and conjugate with graphene to form π–π bonds, such that it can effectively increase the thermal stability and then couple with Pd^{2+}.[43–45] The Pd nanoparticles are obtained *in situ* by adding hydrazine hydrate, and the carboxyl group is also reduced to the hydroxyl group. The FTIR spectra shows a characteristic diffraction peak at 1552 cm^{-1}, corresponding to the stretching vibration of ν(–C–O–C–) (Fig. S1†).[46] Moreover, the peak at near 3430 cm^{-1} has a wide and strong absorption, which can be attributed to ν(–OH) stretching vibration.[47] The ν(–OH) absorption peak intensity decreases until its value is almost zero; this indicates that oxygen in its elemental state (O_2) is still present despite the thermal treatment. Moreover, although there are two peaks at 1203 cm^{-1} and 1142 cm^{-1}, which belong to the vibration of ν(–C–O), only the 1203 cm^{-1} absorption peak experiences a red shift because the hydrogen ion of gallic acid is beneficial to enhance the conjugation between benzene and the oxygen atom.[48]

As evidenced by the X-ray diffraction (XRD) pattern shown in Fig. 1a, the diffraction peaks for graphite within the samples are well-indexed to the spinel structure (PDF No. 41-1487), whereas the shift in the (002) graphitic diffraction peak at 24.3° verifies the successful carbonization of N-doped graphene.[49] Moreover, the presence of Pd is confirmed by the peaks present at 2θ of 40.1°, 46.7°, and 68.1°, which originate from the (111), (200), and (220) diffraction of Pd, respectively, which can be ascribed to the face-centered cubic-phases of Pd (fcc).[50] The sharp diffraction peaks of Pd reveal the high degree of crystallinity of the Pd nanoparticles. The characteristics of the N-doped carbon in the obtained product are further analyzed by Raman spectroscopy. Moreover, the presence of graphitic carbon was confirmed by the analysis of the Raman spectrum shown in Fig. 1b. Herein, two characteristic peaks of carbon materials are present, located at 1369 cm^{-1} and 1589 cm^{-1}, corresponding to the D and G bands, respect-

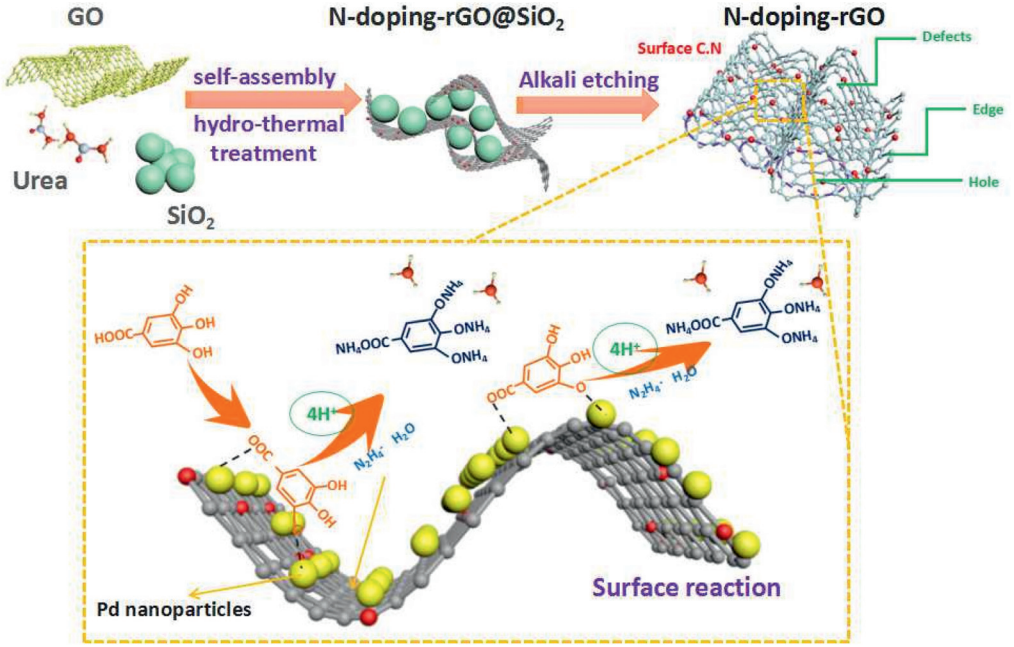

Scheme 1 Schematic of the synthesis process for GN@Pd-GA.

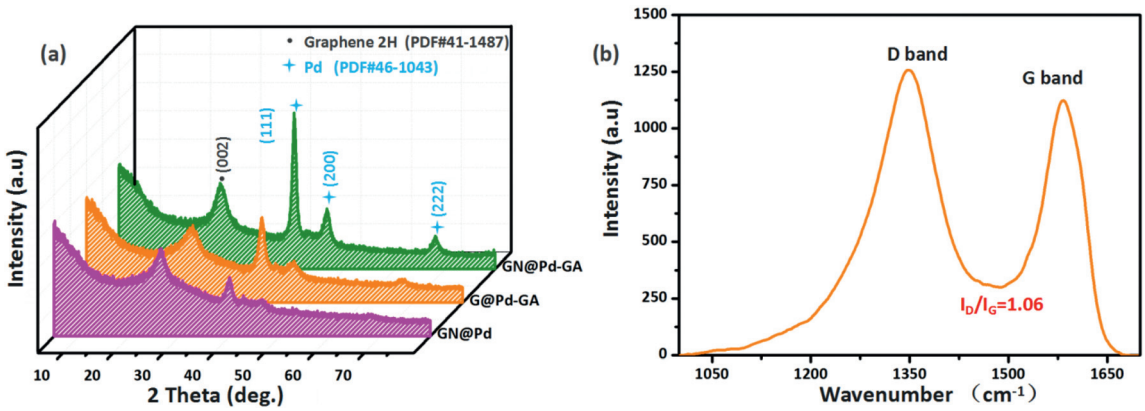

Fig. 1 (a) X-ray diffraction of the as-synthesized samples and (b) Raman pattern of GN@Pd-GA.

ively. It is well-documented that the D band is associated with defects and induced disorder, whereas the G band is derived from sp^2 hybridized carbon.[51] The peak intensity ratio of the D band to the G band (I_D/I_G) is related to the degree of disordering during the graphitization of carbon materials (Fig. S11†). The value of I_D/I_G for the GN@Pd-GA material is calculated to be 1.06, and the I_D/I_G value of rGO is calculated to 0.91: the increase in I_D/I_G value further implies a major disorder in the carbon lattice.

The microstructure is related to the type of pores for mass transport of the graphite carbons. The N_2 sorption isotherm illustrated in Fig. 2 shows the presence of abundant mesopores within GN@Pd-GA, which is created by doping N and subsequent decomposition of the SiO_2 sacrificial template. Mesopores with different diameters can be found in the BJH

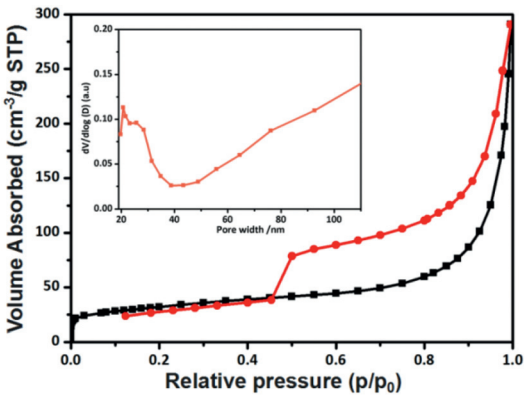

Fig. 2 The nitrogen adsorption–desorption isotherm for GN@Pd-GA (the inset shows the corresponding pore size distribution spectrum).

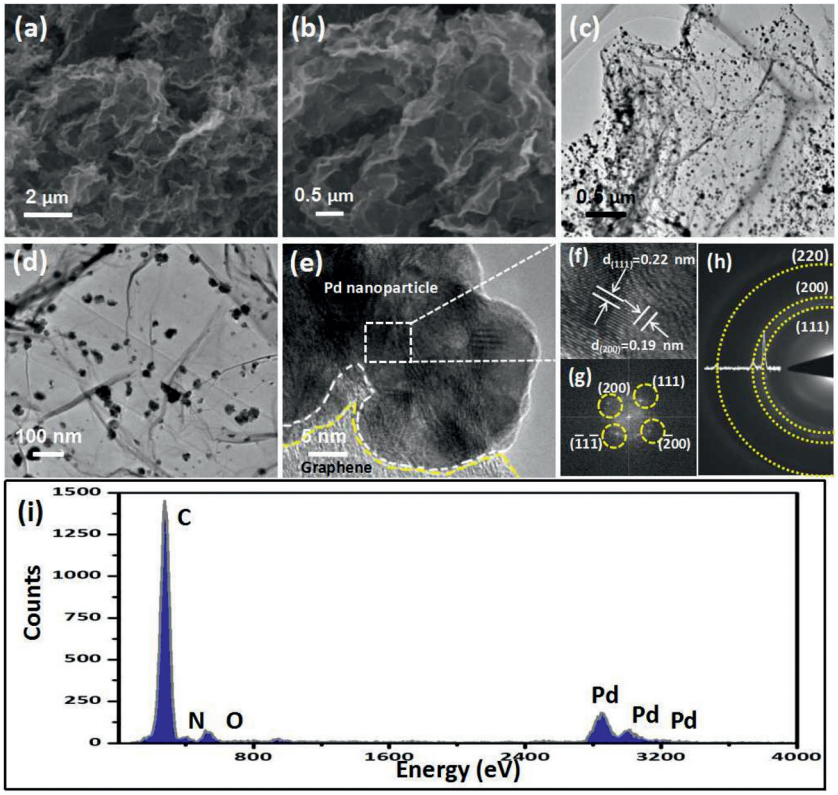

Fig. 3 (a, b) The SEM images of GN@Pd-GA; (c, d) TEM images of GN@Pd-GA; and (e) high-resolution TEM image; (f–h) SAED patterns of GN@Pd-GA; and (i) X-ray photoelectron spectroscopy of GN@Pd-GA.

pore size distribution (the inset of Fig. 2) of GN@Pd-GA. The GN@Pd-GA also exhibited a high Brunauer–Emmett–Teller (BET) surface area (113 $m^2\ g^{-1}$), with a total pore volume of 0.384 $cm^3\ g^{-1}$. The representative SEM and TEM images of GN@Pd-GA are shown in Fig. 3. The panoramagram in Fig. 3 (a and b) illustrates that the as-synthesized sample is a multiple-layer structure. In addition, the GN@Pd sample without gallic acid only possesses a few Pd nanoparticles; this demonstrates the importance of utilizing gallic acid to increase the adhesion of the Pd nanoparticles (Fig. S2†). Detailed structural characteristics of GN@Pd-GA were further investigated by TEM. In addition to the above mentioned SEM images, the TEM images displayed in Fig. 3(c–e) further confirmed that thin layer graphene sheets were successfully synthesized, and Pd nanoparticles were uniformly loaded onto the N-doped graphene. More importantly, a well-defined lattice fringe is observed in Fig. 3f, where the lattice pattern values of 0.22 nm and 0.19 nm corresponding to the (111) and (200) crystal faces of Pd further verify the formation of Pd. The corresponding electron diffraction patterns in Fig. 3(g and h) also indicate the crystal nature of the formed Pd.[52] The EDS analysis of GN@Pd-GA in Fig. 3i shows that different elements have different binding energies; combined with the calculated data (Table S1†), it can be seen that the Pd nanoparticles have been loaded with a weight percentage of 10.23% Pd, which conforms to the addition and the existence of nitrogen in the as-synthesized N-doped graphene with the weight of 2.32%.

To understand the electrochemical activity of the as-synthesized catalytic materials, linear polarization with a rotated disc electrode (RDE) at a scan rate of 10 mV s^{-1} in an oxygen saturated 0.1 mol L^{-1} KOH electrolyte was used to predict the ORR performance. The commercial Pt/C was also tested under the same conditions for comparison.[53] Fig. 4a shows the CV (cyclic voltammetry) curves of the samples. Compared with G@Pd-GA and GN@Pd, GN@Pd-GA exhibits the approached electrochemical surface area comparable to that of commercial Pt/C. In addition, the CV curves obtained under N_2-saturation and O_2-saturation at a scan rate of 10 mV s^{-1} are shown in Fig. S3† and provide evidence that GN@Pd-GA possesses high activity under oxygen saturation. To gain further insights into the positive effects, the ORR performances of samples were evaluated by linear sweep voltammetry (LSV) curves at 1600 rpm (Fig. 4b). The G@Pd-GA exhibited an open circuit potential (0.59 V *vs.* SCE) with a current density of −4.03 mA cm^{-2} at −0.6 V.

GN@Pd showed an open circuit potential (0.57 V *vs.* SCE) with a current density of −3.10 mA cm^{-2} at −0.6 V, and GN@Pd-GA displayed a positive ORR open circuit potential (0.62 V *vs.* SCE) and a current density of −4.43 mA cm^{-2} at −0.6 V, which was remarkably close to those of Pt/C (open circuit potential of 0.65 V with a current density of −4.51 mA

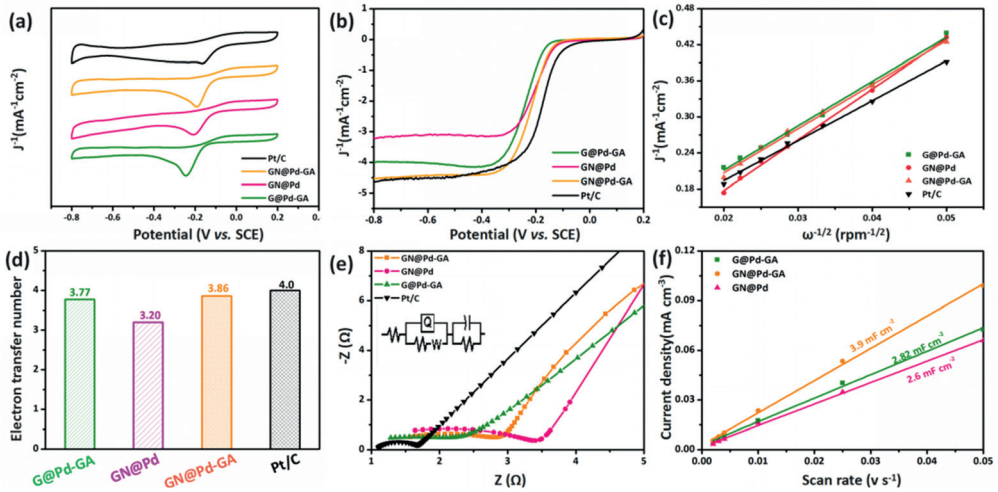

Fig. 4 (a) CV curves of the catalysts in an O_2-saturated 0.1 M KOH solution at the scan rate of 10 mV s^{-1}; (b) LSV curves of catalysts in a 0.1 M KOH solution at the scan rate of 5 mV s^{-1} with 1600 rpm; (c) K–L curves, (d) electron transfer number, (e) Nyquist curves, and (f) the C_{DL} curves of G@Pd-GA, GN@Pd, GN@Pd-GA, and Pt/C.

cm^{-2} at −0.6 V) (Table S2†). Theoretically, the larger the opening potential of the catalyst, the more difficult it is to be corroded. More details are proposed to further evaluate the complex ORR process. The Koutecky–Levich (K–L) curves (j^{-1} *vs.* $\omega^{-1/2}$) of catalysts in Fig. 4c were used to calculate the transfer number (n) of kinetics under the current at −0.6 V in the system of saturated oxygen, and the LSV curves of the catalysts showed good linearity at various rotation speeds (Fig. S4†).[35] As shown in Fig. 4d, the n value of the target material for GN@Pd-GA was calculated to be 3.86, which was close to the value of Pt/C (4.00). Obviously, the value of n of GN@Pd-GA was much larger than those of GN@Pd (3.2) and G@Pd-GA (3.77). It is well known that the oxygen reduction reaction is usually dependent on the transport pathway of 2 e^- or 4 e^- reduction.[54] Therefore, we can conclude that the layered nitrogen-doped graphene provides an effective surface for electron transport and increases the electron donation effect of the nitrogen atom and the alkalinity of the *ortho*-carbon atoms to further greatly provide more active sites for the ORR process.

To further investigate the conductivity and electrochemical surface active area (ECSA) of the catalysts, electrochemical independence spectrum (EIS) and CV spectra were obtained for the ORR catalyst. Clearly, the GN@Pd-GA has a lower R_{ct} than GN@Pd (which did not utilize gallic acid) (Fig. 4e and Table S3†). The obtained results indicated that the great conductivity of GN@Pd-GA catalyst was attributed to the use of gallic acid as the conjugated plane contributed to accelerating the charge transfer rate. In addition, the defects of N-doped graphene can increase R_{ct} and slow down the electron transfer. The double layer capacitance (C_{DL}) curves in the CV curves (Fig. S5†) obtained under various scan rates in Fig. 4f reveal that the elctrochemically active area increases with the addition of N in graphene and in the distributed Pd particles. The durability of the obtained GN@Pd-GA was also evaluated by the chronoamperometric response at a constant cathodic voltage of −0.3 V (*vs.* SCE) in an O_2-saturated 0.1 M KOH. As shown in Fig. 5a, the tolerance of methanol of GN@Pd-GA exhibited a stronger resistance and better selectivity of methanol as compared to that of Pt/C; this was likely due to the synergy effects between the Pd nanoparticles and rGO. To ensure sustained long-term performance from Fig. 5b, the current density of the as-prepared cathode showed a reduction of 11.18% after 20 000 s, whereas Pt/C had lost almost 18.9% of current, indicating the excellent stability of GN@Pd-GA.

To compare the different cathodes (within MFCs), the performances of single-chamber MFCs equipped with the different catalysts were examined. Fig. 6a shows the redox process of the MFCs device assembled with a GN@Pd-GA cathode in a sewage medium. The maximum output voltage of the cathode catalysts is also shown in Fig. 6b and clearly reveals that the GN@Pd-GA possesses the relatively high value of 0.4 ± 0.02 V. Furthermore, the power density of the GN@Pd-GA cathode is 391.06 mW m^{-2} (Fig. 6c), which is slightly lower than that of Pt/C (406.65 mW m^{-2}) (Table S4†). Impressively, the increased number of active sites and the well-dispersed Pd particles can contribute to greatly improve the electric power density. Fig. 6d also shows polarization curves originating from the MFCs equipped with electrocatalysts, confirming the rate-determining step in the ORR process. Therefore, the excellent ORR activity of the GN@Pd-GA cathode is mainly attributed to three factors: (i) the small size and high dispersion of Pd nanoparticles decorated on the porous N-rGO can provide excellent conductivity, large ECSA (depends on the values of C_{DL}), and abundant active sites by the assisted synthesis using gallic acid; (ii) the robust stability of GN@Pd-GA may be mainly due to the porous N-rGO; and (iii) the synergistic effect between Pd and N-rGO can also be beneficial to the improvements of the electrocatalytic activity for GN@Pd-GA.

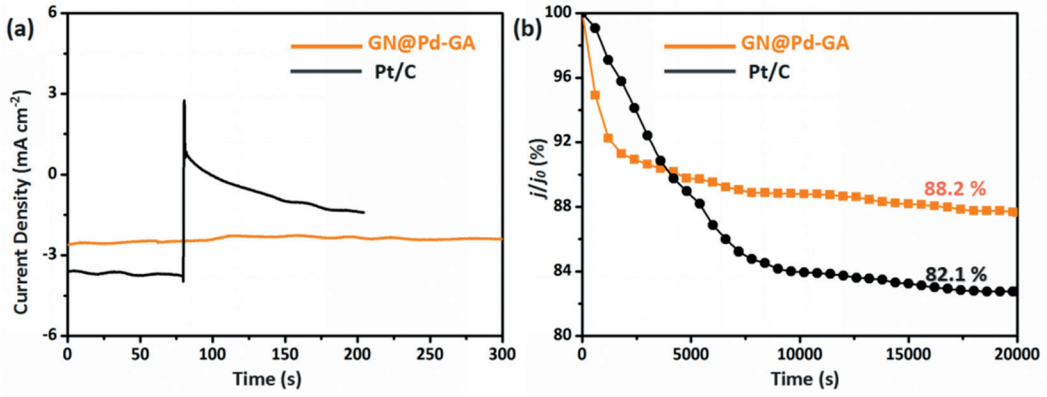

Fig. 5 (a) Chronoamperometric responses to the injection of methanol into an O_2-saturated 0.1 M KOH solution at the GN@Pd-GA and Pt/C electrodes in −0.3 V; (b) chronoamperometric responses of the GN@Pd-GA and Pt/C electrodes at −0.6 V (*vs.* SCE) in O_2-saturated 0.1 M KOH solutions at a rotation rate of 1600 rpm.

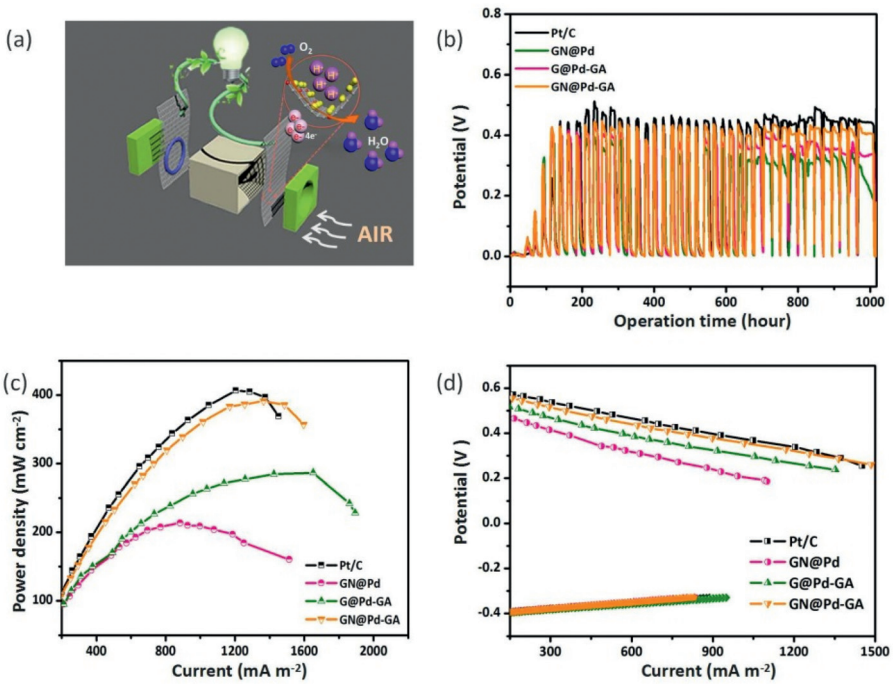

Fig. 6 (a) Schematic of the ORR process in the MFCs; (b) maximum cell voltages; (c) power density curves; and (d) entire cells and anode (*vs.* Ag/AgCl) polarization curves for different catalyst materials.

Conclusion

In summary, well-dispersed Pd nanoparticles anchored on N-rGO have been successfully synthesized through a facile self-assembly and solvothermal method with the assistance of gallic acid. The as-synthesized GN@Pd-GA exhibits a remarkable ORR performance, nearly comparable to that of commercial Pt/C. The excellent ORR performance may be mainly attributed to the efficient synergistic effect between Pd and porous N-rGO. Most importantly, the MFCs equipped with the GN@Pd-GA cathode catalyst accordingly displays preferable stability and power density. This study demonstrates a promising strategy to develop Pd with enhanced catalytic efficiency for energy conversion reactions.

Conflicts of interest

There are no conflicts to declare.

Acknowledgements

This work was supported by the Natural Science Foundations of China (Grant No. 21576056, and 21576057), Guangdong

Natural Science Foundation (Grant No. 2015A030313503 and 2017A030311016), Science and Technology Research Project of Guangdong Province (Grant No. 2016A010103043), Featured Innovation Project of Guangdong University (Grant No. 2016KTSCX107), Science and Technology Research Project of Guangzhou (Grant No. 201607010232, 201607010198, 201607010263), Guangzhou University's 2017 Training Program for Young Top-Notch Personnel (BJ201704), and High Level University Construction Project (Regional Water Environment Safety and Water Ecological Protection).

References

1 S. Chu, Y. Cui and N. Liu, *Nat. Mater.*, 2016, **16**, 16–22.
2 G. F. Chen, X. X. Li, L. Y. Zhang, N. Li, T. Y. Ma and Z. Q. Liu, *Adv. Mater.*, 2016, **28**, 7680–7687.
3 C. Y. Su, H. Cheng, W. Li, Z. Q. Liu, N. Li, Z. Hou, F. Q. Bai, H. X. Zhang and T. Y. Ma, *Adv. Energy Mater.*, 2017, **7**, 1602420.
4 M. V. Kannan and G. Gnana Kumar, *Biosens. Bioelectron.*, 2016, **77**, 1208–1220.
5 H. Yuan, Y. Hou, I. M. Abu-Reesh, J. Chen and Z. He, *Mater. Horiz.*, 2016, **3**, 382–401.
6 V. R. Stamenkovic, D. Strmcnik, P. P. Lopes and N. M. Markovic, *Nat. Mater.*, 2016, **16**, 57–69.
7 S. Hussain, H. Erikson, N. Kongi, M. Merisalu, P. Ritslaid, V. Sammelselg and K. Tammeveski, *Int. J. Hydrogen Energy*, 2017, **42**, 5958–5970.
8 P. Moni, S. Hyun, A. Vignesh and S. Shanmugam, *Chem. Commun.*, 2017, **53**, 7836–7839.
9 X. Xia, J. L. R. Yates, G. Jones, M. Sarwar, I. Harkness and D. Thompsett, *J. Mater. Chem. A*, 2016, **4**, 15181–15188.
10 Q. Zhao, Q. Wang, Y. Su, K. Huang, G. Xu, Y. Li, J. Liu, B. Liu and J. Zhang, *CrystEngComm*, 2017, **19**, 4964–4971.
11 V. Petkov, B. Prasai, S. Shan, Y. Ren, J. Wu, H. Cronk, J. Luo and C. J. Zhong, *Nanoscale*, 2016, **8**, 10749–10767.
12 W. Wang, Z. Wang, J. Wang, C. J. Zhong and C. J. Liu, *Adv. Sci.*, 2017, **4**, 1600486.
13 B. B. Xiao, X. B. Jiang and Q. Jiang, *Phys. Chem. Chem. Phys.*, 2016, **18**, 14234–14243.
14 K. Yang, P. Jiang, J. Chen and Q. Chen, *ACS Appl. Mater. Interfaces*, 2017, **9**, 32106–32113.
15 S. Noh and J. H. Shim, *RSC Adv.*, 2016, **6**, 84334–84341.
16 K. Mohanraju, G. Kousik and L. Cindrella, *New J. Chem.*, 2016, **40**, 8681–8695.
17 Y. Holade, R. G. da Silva, K. Servat, T. W. Napporn, C. Canaff, A. R. de Andrade and K. B. Kokoh, *J. Mater. Chem. A*, 2016, **4**, 8337–8349.
18 M. D. Mobarakeh, *Fibers Polym.*, 2017, **18**, 95–101.
19 M. Wang, X. Qin, K. Jiang, Y. Dong, M. Shao and W.-B. Cai, *J. Phys. Chem. C*, 2017, **121**, 3416–3423.
20 A. Esfandiari, M. Kazemeini and D. Bastani, *Int. J. Hydrogen Energy*, 2016, **41**, 20720–20730.
21 L. Bu, N. Zhang, S. Guo, X. Zhang, J. Li, J. Yao, T. Wu, G. Lu, J.-Y. Ma, D. Su and X. Huang, *Science*, 2016, **354**, 1410–1414.
22 F. He, K. Li, C. Yin, Y. Wang, H. Tang and Z. Wu, *Carbon*, 2017, **114**, 619–627.
23 S. H. A. Miller, M. Bellini, F. Vizza, C. Hasenöhrl and R. D. Tilley, *Catal. Sci. Technol.*, 2016, **6**, 6870–6878.
24 X. Wang, M. Vara, M. Luo, H. Huang, A. Ruditskiy, J. Park, S. Bao, J. Liu, J. Howe, M. Chi, Z. Xie and Y. Xia, *J. Am. Chem. Soc.*, 2015, **137**, 15036–15042.
25 N. Zhang, Y. Feng, X. Zhu, S. Guo, J. Guo and X. Huang, *Adv. Mater.*, 2017, **29**, 1603774.
26 Y. Jiang, Y. Yan, Y. Han, H. Zhang and D. Yang, *RSC Adv.*, 2017, **7**, 43373–43379.
27 X. Quan, Y. Mei, H. Xu, B. Sun and X. Zhang, *Electrochim. Acta*, 2015, **165**, 72–77.
28 D. W. Chang and J.-B. Baek, *J. Mater. Chem. A*, 2016, **4**, 15281–15293.
29 W. Miran, M. Nawaz, J. Jang and D. S. Lee, *RSC Adv.*, 2016, **6**, 91314–91319.
30 X. Meng, C. Yu, X. Song, Y. Liu, S. Liang, Z. Liu, C. Hao and J. Qiu, *Adv. Energy Mater.*, 2015, **5**, 1500180.
31 R. K. Gautam, H. Bhattacharjee, S. Venkata Mohan and A. Verma, *RSC Adv.*, 2016, **6**, 110091–110101.
32 L. Zhang, Q. Chang, H. Chen and M. Shao, *Nano Energy*, 2016, **29**, 198–219.
33 L. Tan, Y. D. Yang, N. Li, S. Chen and Z. Q. Liu, *Catal. Sci. Technol.*, 2017, **7**, 1315–1323.
34 X.-W. Xie, J. J. Lv, L. Liu, A. J. Wang, J. J. Feng and Q.-Q. Xu, *Int. J. Hydrogen Energy*, 2017, **42**, 2104–2115.
35 S. Williams, Jr. Hummers and E. Richarde, *J. Am. Chem. Soc.*, 1958, **80**, 1339.
36 L. Tan, N. Li, S. Chen and Z.-Q. Liu, *J. Mater. Chem. A*, 2016, **4**, 12273–12280.
37 W. Y. Xia, L. Tan, N. Li, J. C. Li and S.-H. Lai, *J. Mater. Sci.*, 2017, **52**, 7539–7545.
38 J. Fan, K. Qi, H. Chen, W. Zheng and X. Cui, *J. Colloid Interface Sci.*, 2017, **490**, 190–196.
39 L. Y. Jiang, X. X. Lin, A. J. Wang, J. Yuan, J. J. Feng and X.-S. Li, *Electrochim. Acta*, 2017, **225**, 525–532.
40 K. Qi, Q. Wang, W. Zheng, W. Zhang and X. Cui, *Nanoscale*, 2014, **6**, 15090–15097.
41 L. Shi, A. Wang, T. Zhang, B. Zhang, D. Su, H. Li and Y. Song, *Phys. Chem. Chem. Phys.*, 2013, **117**, 12526–12536.
42 H. Duan and C. Xu, *Phys. Chem. Chem. Phys.*, 2016, **18**, 4166–4173.
43 Y. X. Xu, Z. Y. Lin, X. Q. Huang, Y. Wang, Y. Huang and X. Duan, *Adv. Mater.*, 2013, **25**, 5779–5784.
44 H. Huang, P. Li, M. Zhang, Y. Yu, Y. Huang, H. Gu, C. Wang and Y. Yang, *Nanoscale*, 2017, **9**, 5044–5048.
45 Z. Yu, B. Wang, Y. Li, D. Kang, Z. Chen and Y. Wu, *RSC Adv.*, 2017, **7**, 22599–22609.
46 C. Hu and L. Dai, *Adv. Mater.*, 2017, **29**, 1604942.

47 C. Xu, L. Shi, L. Guo, X. Wang, X. Wang and H. Lian, *J. Appl. Polym. Sci.*, 2017, **134**, 45345.
48 J. Zhang, Y. Liu, H. Guan, Y. Zhao and B. Zhang, *J. Alloys Compd.*, 2017, **721**, 731–740.
49 H. Song, L. Shen, J. Wang and C. Wang, *Nano Energy*, 2017, **34**, 47–57.
50 Q. Zhang, S. Ye, X. Chen, X. Song, L. Li and X. Huang, *Appl. Catal., B*, 2017, **203**, 673–683.
51 G. Zhang, W. Lu, L. Cao, X. Qin, F. Ding, S. Tang, Z.-G. Shao and B. Yi, *J. Power Sources*, 2016, **326**, 23–34.
52 N. An, Y. An, Z. Hu, B. Guo, Y. Yang and Z. Lei, *J. Mater. Chem. A*, 2015, **3**, 22239–22246.
53 L. Sun, B. Liao, X. Ren, Y. Li, P. Zhang, L. Deng and Y. Gao, *Electrochim. Acta*, 2017, **235**, 543–552.
54 N. M. Wilson and D. W. Flaherty, *J. Am. Chem. Soc.*, 2016, **138**, 574–586.